

## Articles

# SPONTANEOUS IMBIBITION OF A WETTING FLUID INTO A FRACTURE WITH OPPOSING FRACTAL SURFACES: THEORY AND EXPERIMENTAL VALIDATION

J. W. BRABAZON,<sup>\*</sup> E. PERFECT,<sup>\*,¶</sup> C. H. GATES,<sup>\*</sup> L. J. SANTODONATO,<sup>†</sup>  
I. DHIMAN,<sup>‡</sup> H. Z. BILHEUX,<sup>‡</sup> J.-C. BILHEUX,<sup>§</sup> and L. D. MCKAY<sup>\*</sup>

*<sup>\*</sup>Department of Earth and Planetary Sciences  
University of Tennessee, Knoxville, TN 37996, USA*

*<sup>†</sup>Instrument and Source Division  
Oak Ridge National Laboratory, Oak Ridge, TN 37831, USA*

*<sup>‡</sup>Chemical and Engineering Materials Division  
Oak Ridge National Laboratory, Oak Ridge, TN 37831, USA*

*<sup>§</sup>Neutron Data Analysis and Visualization Division  
Oak Ridge National Laboratory, Oak Ridge, TN 37831, USA*

*<sup>¶</sup>eperfect@utk.edu*

Received March 17, 2018

Accepted May 29, 2018

Published September 7, 2018

### Abstract

Spontaneous imbibition (SI) is a capillary-driven flow process, in which a wetting fluid moves into a porous medium displacing an existing non-wetting fluid. This process likely contributes to the loss of fracking fluids during hydraulic fracturing operations. It has also been proposed as a method for an enhanced recovery of hydrocarbons from fractured unconventional reservoirs. Numerous analytical and numerical approaches have been employed to model SI. Invariably, these idealize a fracture as the gap formed between parallel flat surfaces. In reality, rock fracture surfaces are rough over multiple scales, and this roughness will influence the contact angle and

---

<sup>¶</sup>Corresponding author.

This is an Open Access article published by World Scientific Publishing Company. It is distributed under the terms of the Creative Commons Attribution 4.0 (CC-BY) License. Further distribution of this work is permitted, provided the original work is properly cited.

rate of fluid uptake. We derived an analytical model for the early-time SI behavior within a fracture bounded by parallel impermeable surfaces with fractal roughness assuming laminar flow. The model was tested by fitting it to experimental data for the SI of deionized water into air-filled rock fractures. Twenty cores from two rock types were investigated: a tight sandstone (Crossville) and a gas shale (Mancos). A simple Mode I longitudinal fracture was produced in each core by compressive loading between parallel flat plates using the Brazilian method. Half of the Mancos cores were fractured perpendicular to bedding, while the other half were fractured parallel to bedding. The two main parameters in the SI model are the mean separation distance between the fracture surfaces,  $\bar{x}$ , and the fracture surface fractal dimension  $2 \leq D < 3$ . The  $\bar{x}$  was estimated for each core by measuring the geometric mean fracture aperture width through image analysis of the top and bottom faces, while  $D$  was estimated inversely by fitting the SI model to measurements of water uptake obtained using dynamic neutron radiography. The  $\bar{x}$  values ranged from  $45 \mu\text{m}$  to  $190 \mu\text{m}$ , with a median of  $93 \mu\text{m}$ . The SI model fitted the height of uptake versus time data very well for all of the rock cores investigated; medians of the resulting root mean squared errors and coefficients of determination were  $0.99 \text{ mm}$  and  $0.963$ , respectively. Estimates of  $D$  ranged from  $2.04$  to  $2.45$ , with a median of  $2.24$ . Statistically, all of the  $D$  values were significantly greater than two, confirming the fractal nature of the fracture surfaces. Future research should focus on forward prediction through independent measurements of  $D$  and extension of the existing SI model to late times (through the inclusion of gravity) and fractures with permeable surfaces.

*Keywords:* Brittle Fracture; Capillarity; Contact Angle; Neutron Radiography; Surface Fractal Dimension; Surface Roughness; Tortuosity.

## 1. INTRODUCTION

Unconventional reservoirs are oil and/or gas producing rock formations that require the implementation of enhanced recovery methods to be commercially viable. They include low permeability gas shale's and tight gas sandstones, and are of growing economic importance.<sup>1,2</sup> The development of hydraulic fracturing, or "fracking", technology has been the key to exploiting unconventional reservoirs. This method is based on horizontal drilling, and involves the injection of large volumes of water, chemical additives, and suspended solids ("proppants") into the subsurface at high pressures.<sup>3</sup> As a result, fractures are induced within the source rocks, increasing their overall permeability.<sup>4</sup> The high rates of flow within the interconnected network of fractures facilitate more efficient recovery of oil and/or gas.

Spontaneous imbibition (SI) is a capillary-driven flow process, in which a wetting fluid (e.g. water, brine) moves into a porous medium displacing a preexisting non-wetting fluid (e.g. air, natural gas, oil).<sup>5-7</sup> This process, using water or brine with added surfactants to displace oil, has been proposed as an enhanced recovery technique.<sup>8,9</sup> With the rapid growth and implementation of fracking technology, SI is now being investigated as a method of improving the recovery of hydrocarbon resources

from fractured unconventional reservoirs.<sup>10,11</sup> SI may also contribute to the loss of fracking fluids (known as "leakoff") during hydraulic fracturing operations.<sup>12</sup>

Numerous analytical and numerical approaches have been proposed for modeling the SI of a wetting fluid into the gap formed by parallel planar surfaces.<sup>5,13-15</sup> However, these models invariably represent the opposing surfaces of the fracture as smooth and flat. In reality, rock fracture surfaces are rough over multiple scales, and this roughness likely influences the contact angle and rate of fluid uptake within the fracture. Fractal geometry is a quantitative paradigm for simulating and characterizing the irregularity of natural systems.<sup>16</sup> Cai *et al.*<sup>17</sup> developed a fractal model to predict the displacement of a non-wetting fluid by a wetting fluid within a tortuous capillary tube. Several studies have shown that rock fracture surfaces exhibit fractal roughness over length scales of two or more orders of magnitude.<sup>18-21</sup> However, we were unable to find any previously published studies that have sought to incorporate the fractal roughness of fracture surfaces into a model for the prediction of SI.

The objective of this paper is to derive an analytical model for the SI mechanism within a fracture bounded by parallel rough fractal surfaces. The model will be tested by fitting it to experimental

data for the SI of water into air-filled fractured rock cores collected using neutron radiography.

## 2. THEORY

The well-known Wenzel equation<sup>22</sup> for the contact angle of a fluid on a rough surface,  $\theta_R$ , is given by

$$\cos \theta_R = r \cos \theta_S, \quad (1)$$

where  $\theta_S$  = the contact angle of a fluid on a smooth flat surface, and  $r$  is the roughness ratio defined as

$$r = \frac{A_R}{A_S}, \quad (2)$$

where  $A_R$  = the projected area of the rough surface relative to the corresponding area of the smooth flat surface,  $A_S$ .

Assuming that the rough surface is fractal, the number,  $N$ , of tiles of length,  $\ell$ , needed to cover it can be calculated using the following expression<sup>23,24</sup>:

$$N = \left(\frac{\mathcal{L}}{\ell}\right)^D, \quad (3)$$

where  $\mathcal{L}$  = the length scale corresponding to the maximum extent of fractal scaling, and  $2 \leq D < 3$  is the surface fractal dimension. Based on Eq. (3), the area of a rough fractal surface of length  $\mathcal{L}$  is given by

$$A_R = \ell^2 N = \ell^{2-D} \mathcal{L}^D. \quad (4)$$

Based on Euclidean geometry, the area of a smooth flat surface of length  $\mathcal{L}$  is given by

$$A_S = \mathcal{L}^2. \quad (5)$$

Substituting Eqs. (4) and (5) into Eq. (2), we obtain

$$r = \left(\frac{\ell}{\mathcal{L}}\right)^{2-D}. \quad (6)$$

Substituting Eq. (6) into Eq. (1), we obtain the following expression for the contact angle of a fluid on a rough fractal surface:

$$\cos \theta_R = \left(\frac{\ell}{\mathcal{L}}\right)^{2-D} \cos \theta_S. \quad (7)$$

Equations (1)–(7) provide a new, parsimonious derivation of Hazlett's equation<sup>25</sup> for the contact angle of a fluid on a rough fractal surface. Hazlett's equation<sup>25</sup> was written in terms of area scaling limits instead of length scaling limits, i.e.

$$\cos \theta_R = \left(\frac{\sigma_L}{\sigma_U}\right)^{1-\frac{D}{2}} \cos \theta_S, \quad (8)$$

where  $\sigma_U$  and  $\sigma_L$  are the upper and lower area limits of fractal scaling, respectively. Comparing Eqs. (7)

and (8), it can easily be seen that they are equivalent, since  $\sigma_U \propto \mathcal{L}^2$  and  $\sigma_L \propto \ell^2$ .

Ignoring gravity, the SI of a wetting fluid into the gap formed between smooth flat impermeable parallel plates is given by<sup>13</sup>

$$L = \sqrt{\frac{x\gamma \cos \theta_{St}}{3\mu}}, \quad (9)$$

where  $L$  = the distance traveled by the wetting front in time,  $t$ ,  $x$  = the separation distance between the two plates,  $\mu$  = the absolute viscosity, and  $\gamma$  = the surface tension of the liquid–vapor interface. Substituting Eq. (7) into Eq. (9) and replacing  $x$  with the mean separation distance between the fracture surfaces,  $\bar{x}$ ,<sup>26</sup> results in the following expression for the SI of a wetting fluid into the gap formed by parallel impermeable fracture surfaces with fractal roughness:

$$L = \sqrt{\frac{\bar{x}\gamma \left(\frac{\ell}{\mathcal{L}}\right)^{2-D} \cos \theta_{Rt}}{3\mu}}. \quad (10)$$

Both Eqs. (9) and (10) assume a laminar flow regime.

It is evident from Eq. (7) (see Fig. 1), that the contact angle for a wetting fluid on a rough fractal surface ( $\theta_R$ ) tends to approach zero for most values of  $\theta_S$ ,  $D$  and  $\frac{\ell}{\mathcal{L}}$  likely to be encountered in geological systems. Thus, it is reasonable to assume that  $\cos \theta_R = 1$  in Eq. (10), i.e.

$$L \approx \sqrt{\frac{\bar{x}\gamma \left(\frac{\ell}{\mathcal{L}}\right)^{2-D} t}{3\mu}}. \quad (11)$$

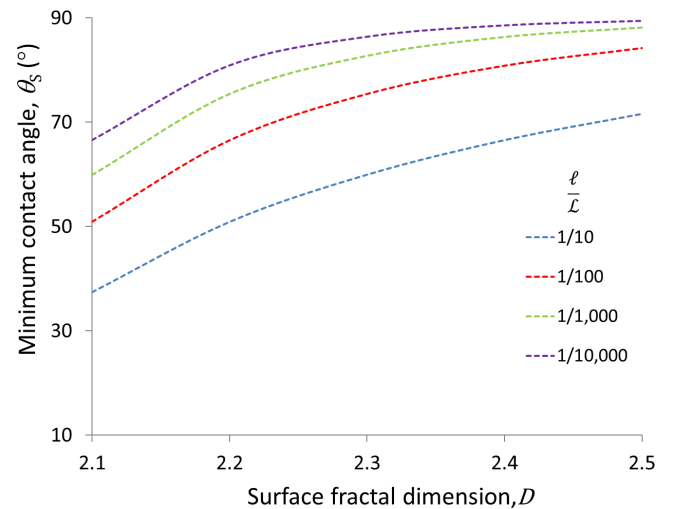


**Fig. 1** Minimum contact angles for a fluid on a smooth flat surface,  $\theta_S$ , required to give  $\theta_R > 0$  on a rough fractal surface predicted using Eq. (7) for various combinations of  $D$  and  $\frac{\ell}{\mathcal{L}}$ .

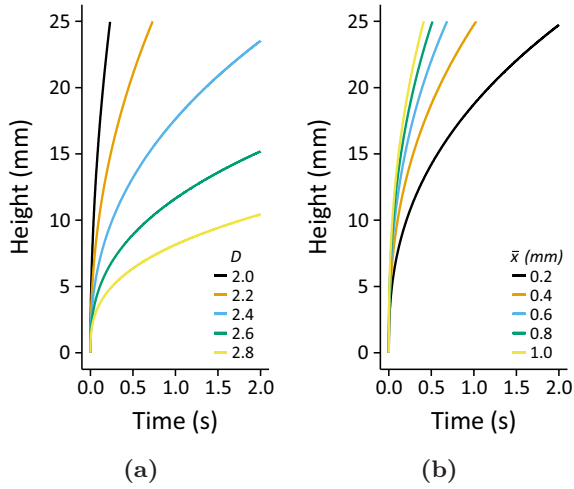


**Fig. 2** Height of wetting within a fracture versus time as predicted by Eq. (12). (a) Fracture aperture spacing,  $\bar{x}$ , held at  $100 \mu\text{m}$  while varying the surface fractal dimension,  $D$ . (b) Surface fractal dimension,  $D$ , held at 2.5 while varying the fracture aperture spacing,  $\bar{x}$ .

Assuming that the distance traveled by the wetting front represents the upper length limit of fractal scaling, i.e.  $L = \mathcal{L}$ , Eq. (11) can be rewritten as

$$L \approx \left( \frac{\bar{x}\gamma}{3\mu\ell^{2-D}} \right)^{\frac{1}{D}} t^{\frac{1}{D}}. \quad (12)$$

The influence of the surface fractal dimension,  $D$  and mean fracture aperture width,  $\bar{x}$ , on rates of water uptake predicted by Eq. (12) are illustrated in Fig. 2. When  $\bar{x}$  is held constant, imbibition rates decrease with increasing values of  $D$  (Fig. 2a); this trend can be attributed to the increase in surface roughness as  $D$  gets larger, resulting in more tortuous flow paths, and possibly turbulent flow,<sup>27</sup> within the fracture. As  $\bar{x}$  is increased with  $D$  held constant, imbibition rates increase (Fig. 2b); this is because flow occurs more easily within a wider channel due to reduced friction with the side walls. It should be noted that these are early time predictions because the current model neglects gravity. As such they are consistent with standard capillary theory, which predicts rapid rates of uptake in large diameter capillary tubes at early times, but lower maximum heights attained relative to smaller diameter capillary tubes at late times.<sup>28</sup>

When applying Eq. (12) in an experimental setting, neutron radiography is used to determine  $L$  and  $t$  (see Sec. 3). However, the time at which the wetting fluid first contacts the base of the fracture is not known precisely. Therefore, when fitting Eq. (12) to experimental data a constant,  $c$ ,

is introduced to account for this uncertainty, i.e.

$$L \approx \left( \frac{\bar{x}\gamma}{3\mu\ell^{2-D}} \right)^{\frac{1}{D}} (t - c)^{\frac{1}{D}}. \quad (13)$$

The unknown parameters, to be estimated by fitting Eq. (13) to experimental  $L$  versus  $t$  data, are  $D$  and  $c$ . The other parameters in Eq. (13),  $\gamma$ ,  $\mu$ ,  $\bar{x}$  and  $\ell$ , are all known quantities;  $\gamma$  and  $\mu$  are physico-chemical constants whose values are tabulated in the literature,  $\bar{x}$  is measured by image analysis (see Sec. 3), and the lower length limit of fractal scaling,  $\ell$ , is taken to be the length of the ruler used for the measurements, i.e. pixel length in neutron radiography.

### 3. MATERIALS AND METHODS

Two rock types with physical properties representative of unconventional reservoir rocks were investigated: a tight sandstone (Crossville) and a gas shale (Mancos). Several core samples (5.08 cm long  $\times$  2.54 cm diameter) of each rock type were supplied by Kocurek Industries Inc. (Caldwell, TX, USA). The samples were cored from surface outcrops with unknown locations. The Crossville sandstone samples were cored parallel to bedding, while the Mancos shale samples were cored both parallel and perpendicular to bedding.

Crossville sandstone (known commercially as ‘‘Crab Orchard sandstone’’) was deposited during the Pennsylvanian period and is located in Kentucky and Tennessee, USA. It is a light-gray fine-to medium-grained sandstone with bands of red, yellow, brown, and gray due to iron staining.<sup>29</sup> Gehne and Benson<sup>30</sup> report that the permeability of Crossville sandstone varies between  $3 \times 10^{-18}$  and  $3 \times 10^{-17} \text{ m}^2$ . The solid phase density and helium gas porosity of the cored samples were measured using the method of Donnelly *et al.*<sup>31</sup> and were determined to be  $2.50 (\pm 0.01) \text{ gcm}^{-3}$  and  $5.85 (\pm 0.27)\%$ , respectively.

The Mancos shale is an interbedded siltstone and shale located in New Mexico, Wyoming, and Utah, USA. It was deposited during the Late Cretaceous and has an estimated 595 billion cubic meters of recoverable gas.<sup>32,33</sup> According to Mokhtari and Tutuncu,<sup>34</sup> the permeability of Mancos shale varies between  $9 \times 10^{-19}$  and  $3 \times 10^{-17} \text{ m}^2$ . The samples investigated were gray in color with light gray interbedding. Their solid phase densities and helium gas porosities were determined, using the method of

Donnelly *et al.*,<sup>31</sup> to be  $2.50 (\pm 0.01) \text{ gcm}^{-3}$  and  $5.59 (\pm 0.39)\%$ , respectively.

Each rock core was wrapped longitudinally with Kapton tape to help maintain the integrity of the sample during fracturing and to create a no-flow boundary for the water uptake experiments. This tape can withstand high temperatures and high pressures, and is free of hydrogen compounds that would otherwise inhibit the neutron radiography. A simple Mode I longitudinal fracture was produced in each wrapped core by compressive loading between parallel flat plates using the Brazilian method.<sup>28,35</sup> The load was applied by manually operating the bottom loading platen of a Carver Laboratory Press (Model M) with a 25 Ton Hydraulic Unit (Model #3925). A distinctive crack sound was heard as soon as the fracture occurred. Loading was then immediately stopped.

Fracture aperture widths were measured on all of the cores. Images of both the top and bottom faces of each fractured core were taken with a high resolution camera. These images were analyzed using ImageJ.<sup>36</sup> The width of the aperture was measured at 10 locations on a randomly-positioned superimposed square grid (see Fig. 3a). The measurement process was then repeated using a second randomly-positioned grid. Both the top and bottom images were analyzed in this way, resulting in 40 width measurements per core. As observed by other researchers,<sup>37,38</sup> these data were log-normally

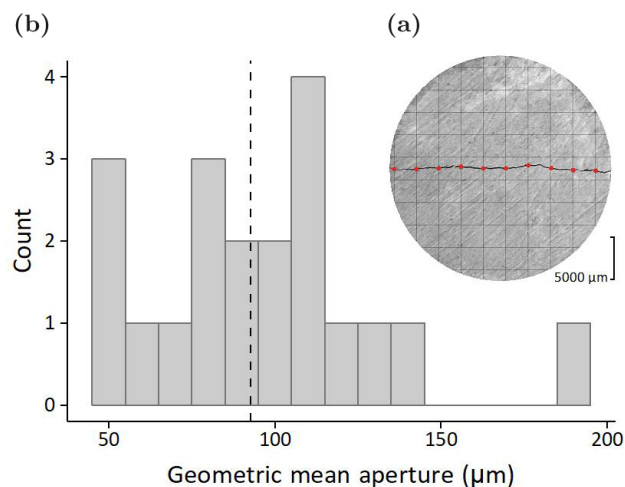


**Fig. 3** (a) A typical fractured Mancos Shale (perpendicular) core shown with a superimposed random grid; measurements of aperture width were taken at the intersection points of the fracture and the grid (shown as red dots). (b) Frequency distribution of geometric mean fracture aperture widths for all of the rock types (20 cores) with a bin size of  $10 \mu\text{m}$ ; the vertical dashed line represents the median value.

distributed. Therefore, the geometric mean fracture aperture width was used as the best estimator of  $\bar{x}$  for each core.

Prior to the SI experiments, all of the cores were oven dried at  $105^\circ\text{C}$  for a period of 24 h to bring them to a zero initial moisture content. The oven-dried cores were then placed into a humidity controlled container to prevent changes in the core's moisture content prior to placement in the neutron beam.

As shown in previous studies,<sup>28,39</sup> neutron imaging allows for distinct visualization of the movement of hydrogen-rich liquids within rocks and other porous media. Thus, dynamic neutron radiography was employed to measure the SI of water within the fractured rock cores. The imaging was performed at Oak Ridge National Laboratory's Neutron Imaging Facility (beam line CG-1D, HFIR). The configuration and specifications of this cold neutron beam line are described in Santodonato *et al.*<sup>40</sup> Neutron radiographs were obtained using the sCMOS detector at a rate of 30 frames per second. The field of view was  $28 \text{ mm} \times 28 \text{ mm}$ , and the spatial resolution was  $100 \mu\text{m}$ . Cores were placed individually in front of the sCMOS detector with their fracture planes oriented parallel to the neutron beam. Each core was imaged as it was brought into contact with a deionized-water reservoir following Cheng *et al.*<sup>28</sup> (Fig. 4a). The resulting uptake of water within the fracture was imaged as a series of time-stamped neutron radiographs.

The radiographs were normalized to ensure visualization of the water (shown as black pixels). To do this, dark-field images were subtracted from radiographs captured both prior to and during wetting. The resulting wetting images were then divided by one of the dry images yielding the final normalized radiographs for each core (Fig. 4b). For each time series of normalized radiographs, a 50 pixel wide transect was superimposed over the fracture from the base of the core to the top of the image. The fracture transect was segmented so as to closely follow any deviations from linearity in the fracture. The total length of the transect,  $L_T$ , was then used to compute the fracture tortuosity,  $\tau$ , using the relationship  $\tau = \frac{L_T}{L_S}$ , where  $L_S$  is the straight line distance between the two ends of the transect.

Pixel gray-scale values were averaged over the width of each superimposed transect, resulting in an average gray-scale pixel value for each pixel length of the transect (Fig. 4c). Change point analysis was employed to determine  $L$  by detecting the distance

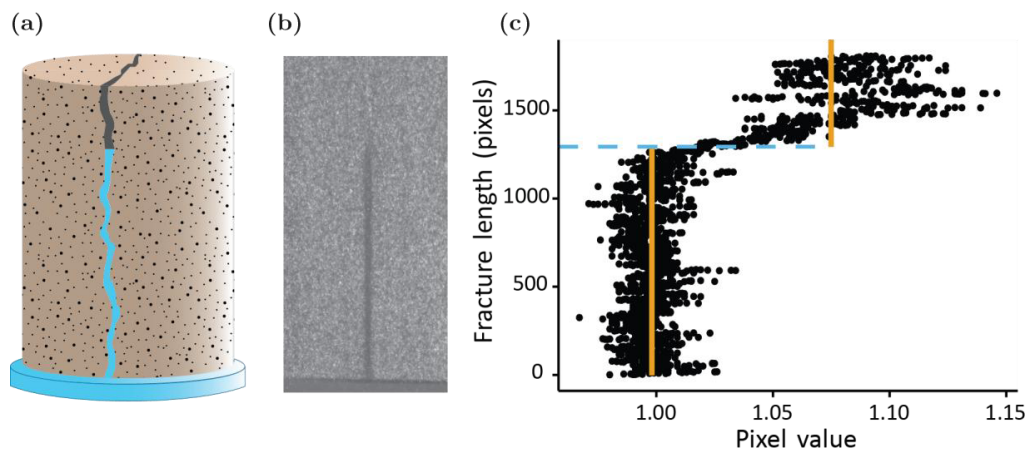


**Fig. 4** (a) Schematic illustration showing the uptake of water within a fractured core sample soon after basal contact with water. (b) Example of a normalized neutron radiograph showing water (in black) within a fractured Crossville Sandstone core. (c) Change point analysis of the neutron radiograph shown in (b). The solid orange lines represent mean pixel values for the wet and dry regions within the fracture. The blue dashed line is the detection point, representing the height of wetting, at which a shift in the mean pixel values occurred.

the water had moved along the transect in each normalized neutron radiograph. Change point analysis can identify abrupt shifts in the statistical properties of a sequence of observations.<sup>41</sup> It is widely used in such fields such as climatology, bioinformatics, and finance.<sup>42–45</sup> We used a single change point model with a likelihood-ratio-based approach, as described by Eckley *et al.*,<sup>41</sup> to detect specific shifts in the mean and variance of the average grayscale pixel values along the fracture transect. The resulting change point for each radiograph in the time series is a mathematical representation of the distance the water has imbibed along the fracture (Fig. 4c). The change points were converted from pixel values to millimeters by comparing the measured diameter of the core in the radiograph to its known diameter. Corresponding  $t$  values were extracted from the radiograph time stamps.

Between 16 and 62 pairs of  $L$  and  $t$  values were collected for each core (Table 1). The surface fractal dimension,  $D$ , and initial imbibition time,  $c$ , were estimated by fitting Eq. (13) to the experimental  $L$  and  $t$  values on a core-by-core basis, with all other parameters specified, using the Levenberg–Marquardt algorithm for non-linear least squares regression estimation.<sup>46</sup> All of the fits converged. Goodness of fit was assessed using the root mean squared error (RMSE) and the coefficient of determination ( $R^2$ ) computed from the observed and predicted values of  $L$  for each core. Non-parametric analyses of variance<sup>47</sup> were performed on the estimated  $D$  and  $c$  parameters, the RMSE's, and the  $\bar{x}$  and  $\tau$  measurements, to

compare median values between the rock groups. Relationships between variables were explored using correlation coefficients ( $r$ ). Statistical significance was assessed at the  $p < 0.05$  level. All of the statistical analyses were performed in the  $R$  software environment.<sup>48</sup>

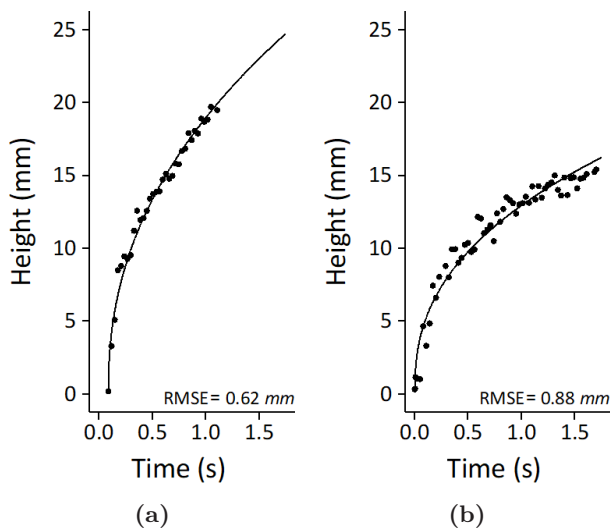
## 4. RESULTS

Geometric mean aperture widths,  $\bar{x}$ , ranged from  $45 \mu\text{m}$  to  $190 \mu\text{m}$ . Their distribution was right skewed, with a median value of  $94 \mu\text{m}$  (Fig. 3b). Among rock groups, the Mancos shale (parallel) cores had the largest variability in  $\bar{x}$ , ranging from  $45 \mu\text{m}$  to  $190 \mu\text{m}$ . For the Mancos shale (perpendicular) cores,  $\bar{x}$  ranged from  $64 \mu\text{m}$  to  $113 \mu\text{m}$ , while for the Crossville sandstone cores, the range was  $79 \leq \bar{x} \leq 111 \mu\text{m}$ . The median  $\bar{x}$  values for the different rock groups were  $87$ ,  $124$ , and  $93 \mu\text{m}$  for Mancos shale (parallel), Mancos shale (perpendicular), and Crossville sandstone, respectively; a Kruskal–Wallis test indicated no significant differences between these values.

The fracture tortuosity's,  $\tau$ , ranged from  $1.000$  to  $1.030$ , with an overall median value of  $1.004$ . A Kruskal–Wallis test indicated significant differences between the median values of  $\tau$  for the different rock groups. The Mancos shale (perpendicular) had the highest median  $\tau$  value ( $1.008$ ), followed by Mancos shale (parallel) ( $1.006$ ), and finally Crossville sandstone ( $1.000$ ). The higher  $\tau$  for Mancos shale (perpendicular) is to be expected since those cores were fractured perpendicular to bedding.

**Table 1** Parameter Estimates and Associated 95% Confidence Intervals Obtained by Fitting Eq. (13) to the Neutron Radiography Data for Each Replicate of Each Rock Group.

Rock Group	Replicate Number	Number of Observations	Surface Fractal Dimension, $D$	Initial Imbibition Time, $c$ (s)	RMSE (mm)
Crossville Sandstone	1	24	$2.21 \pm 0.01$	$0.03 \pm 0.01$	1.03
Crossville Sandstone	2	17	$2.18 \pm 0.02$	$0.03 \pm 0.01$	1.36
Crossville Sandstone	3	34	$2.24 \pm <0.01$	$0.09 \pm <0.01$	0.62
Crossville Sandstone	4	26	$2.19 \pm <0.01$	$0.03 \pm <0.01$	0.52
Crossville Sandstone	5	21	$2.04 \pm 0.01$	$0.01 \pm <0.01$	1.17
Crossville Sandstone	6	24	$2.23 \pm <0.01$	$0.06 \pm <0.01$	0.52
Crossville Sandstone	7	24	$2.24 \pm 0.01$	$0.03 \pm 0.01$	0.80
Mancos Shale (parallel)	1	17	$2.24 \pm 0.01$	$0.03 \pm <0.01$	1.04
Mancos Shale (parallel)	2	58	$2.45 \pm 0.01$	$0.00 \pm <0.01$	0.88
Mancos Shale (parallel)	3	41	$2.35 \pm 0.01$	$0.07 \pm 0.03$	1.43
Mancos Shale (parallel)	4	38	$2.42 \pm 0.02$	$0.01 \pm 0.04$	1.69
Mancos Shale (parallel)	5	16	$2.08 \pm 0.02$	$-0.01 \pm 0.02$	0.95
Mancos Shale (parallel)	6	24	$2.17 \pm 0.01$	$0.01 \pm 0.01$	0.56
Mancos Shale (parallel)	7	46	$2.37 \pm 0.01$	$0.02 \pm 0.03$	1.04
Mancos Shale (perpendicular)	1	23	$2.26 \pm 0.01$	$0.01 \pm <0.01$	0.65
Mancos Shale (perpendicular)	2	60	$2.33 \pm 0.01$	$-0.01 \pm 0.04$	1.04
Mancos Shale (perpendicular)	3	62	$2.29 \pm 0.01$	$-0.06 \pm 0.03$	1.51
Mancos Shale (perpendicular)	4	25	$2.25 \pm 0.02$	$-0.01 \pm 0.05$	1.50
Mancos Shale (perpendicular)	5	13	$2.17 \pm 0.01$	$0.03 \pm <0.01$	0.40
Mancos Shale (perpendicular)	6	17	$2.17 \pm 0.01$	$0.03 \pm <0.01$	0.74

**Fig. 5** Typical height of wetting versus time data sets determined using dynamic neutron radiography and change point analysis: (a) Crossville Sandstone, replicate number 3, and (b) Mancos Shale (cored parallel to bedding), replicate number 2. The solid lines represent predicted values obtained from fitting of Eq. (13) to the experimental data using non-linear regression.

Overall, the fitting of Eq. (13) to the experimental  $L$  versus  $t$  data resulted in excellent correspondence. Typical data sets and fits are shown in Fig. 5. The RMSE, which represents the mean distance of observed values from the predicted values, ranged

from 0.40 mm to 1.69 mm (Table 1). Overall, the median RMSE was 0.99 mm. It is not always easy to comprehend the goodness of fit when reported as an RMSE value. Therefore, although not strictly applicable for non-linear regression, we also computed  $R^2$  values for the individual fits. These ranged from 0.789 to 0.993, with a median  $R^2$  of 0.963. Both the RMSE and  $R^2$  values indicate that the proposed model, Eq. (13), fitted the observed experimental data very well for the 20 rock cores investigated.

The surface fractal dimension,  $D$ , and initial imbibition time,  $c$ , parameters estimated by fitting Eq. (13) to the experimental  $L$  and  $t$  values are listed in Table 1. Among all cores, the median  $D$  value was 2.24, with individual estimates ranging from 2.04 to 2.45. The median  $D$  values for the different rock groups were 2.35, 2.25, and 2.21 for Mancos shale (parallel), Mancos shale (perpendicular), and Crossville sandstone, respectively; there were no significant differences between these values according to a Kruskal–Wallis test. The  $c$  parameter provides an estimate of the time at which the water reservoir first contacted the base of the fractured core. The  $c$  values ranged from  $-0.06$  s to  $0.09$  s, with a median of  $0.02$  s. A Kruskal–Wallis test indicated no significant differences in median  $c$  values among the rock groups.

## 5. DISCUSSION AND CONCLUSIONS

The model presented here, Eqs. (12) and (13), neglects gravity and can only be used to predict early time behavior. To predict the maximum height that a wetting fluid will attain due to SI within a fracture, further research will be required. Specifically, the effect of gravity will need to be incorporated into the theoretical derivation. The current model also assumes that the fracture occurs within an impermeable matrix. This assumption is perfectly reasonable for the low porosity/low permeability rock types investigated in this study.<sup>30,34</sup> There was no visible evidence of water moving into the matrix over the course of the extremely short (<2s) neutron imaging experiments (see Fig. 4b). However, the incorporation of a permeable matrix, allowing for SI of water through the fracture surface, would greatly expand the range of applicability of the proposed model.

At the beginning of the SI process, liquid velocities are relatively high, resulting in large Reynolds numbers. It has been shown that fracture surface roughness can induce turbulent flow at relatively low Reynolds numbers.<sup>27,49</sup> The analytical model we have proposed assumes a laminar flow regime. Therefore, additional investigations are needed to test this assumption and establish critical Reynolds numbers for SI in rough-walled fractures.

As can be seen in Fig. 5, the experimental  $L$  versus  $t$  data were slightly less variable for Crossville sandstone than for Mancos shale. As a result, individual RMSE values obtained from fitting Eq. (13) to the experimental data were generally higher for Mancos shale than for Crossville sandstone (Table 1). The median RMSE for Crossville sandstone was 0.80 mm, as compared to median RMSE's of 1.04 and 0.89 mm for the Mancos shale cores fractured parallel and perpendicular to bedding, respectively. Although not statistically significant (based on a Kruskal–Wallis test), these differences suggest that the model provided a better fit to the sandstone data than to the shale data. This could be due to the presence of more hydrous minerals in the shale samples resulting in darker pixel values during neutron radiography. While the overall trend of wetting could still easily be distinguished in both rock types by change point analysis, the hydrous minerals may have contributed to the variability, and consequently, the higher median RMSE values.

Estimations of the surface fractal dimension,  $D$ , ranged from 2.04 to 2.45 (Table 1). All of the estimates fell within the theoretical bounds of  $2 \leq D < 3$  for a fractal surface, suggesting that our proposed model is physically sound and that rock fracture surfaces are indeed fractal. Recently, Persson<sup>50</sup> has argued that, because of the fragility of actual rough surfaces, practical bounds of  $2 \leq D < 2.3$  apply to such surfaces. The results in Table 1 indicate that 75% of the estimated  $D$  values fell within this restricted range, lending support to his argument.

In the present study, the surface fractal dimension,  $D$ , was estimated inversely by fitting Eq. (13) to experimental wetting height versus time data. However, there is no reason why the fractal model developed here cannot not be used for the forward prediction of water uptake into fractured rocks. To accomplish this,  $D$  would need to be measured independently in future studies. Babadagli and Develi<sup>21</sup> have reported estimates of  $D$  based on fracture surface roughness measurements with a profilometer. Similar measurements could be made following an SI experiment. The fractured core would first be oven dried to remove any retained water. It would then be unwrapped and carefully separated along its fracture plane into two halves, each with an exposed fracture surface. Surface profilometry could then be employed to provide an independent estimate of  $D$  for forward modeling.

The only significant correlation among the variables was a weak positive relationship between  $D$  and  $\bar{x}$  ( $r = 0.53$ ,  $p < 0.05$ ). This trend indicates that the fracture aperture width increased as the fracture surface fractal dimension increased. Assuming random roughness, this is to be expected, since the greater the  $D$  value, the rougher the fracture surfaces and thus, the greater the separation distance between them.

In conclusion, we have developed an analytical model for SI of a wetting fluid into a fracture formed by opposing rough fractal surfaces. The model includes a new parsimonious derivation of Hazlett's equation<sup>25</sup> for the contact angle of a fluid on a rough fractal surface from the well-known Wenzel equation.<sup>22</sup> The model ignores gravity and is applicable to laminar fluid uptake at early times in otherwise impermeable rock. The model was tested by fitting it to experimental data for the SI of deionized water into rock fractures collected using dynamic neutron radiography. Twenty

fractured cores from two rock types (a tight sandstone and a gas shale) were investigated. Geometric mean aperture widths of the fractures,  $\bar{x}$ , were measured and entered into the model, while the surface fractal dimension,  $D$ , was estimated inversely, along with the initial imbibition time,  $c$ . All of the fits successfully converged and there was a close correspondence between the observed and modeled heights of wetting. The estimated  $D$  values ranged from 2.04 to 2.45, with a median value of 2.24, which is reasonable for fracture surfaces with fractal roughness.

## ACKNOWLEDGMENTS

This research was sponsored by the Army Research Laboratory and was accomplished Under Grant No. W911NF-16-1-0043. Portions of this research used resources at the High Flux Isotope Reactor, which is a DOE Office of Science User Facility operated by Oak Ridge National Laboratory. E. Perfect acknowledges support from the Tom Cronin and Helen Sestak Faculty Achievement award. The solid-phase density, dry bulk density, and porosity data were collected by A. D. Vial.

## REFERENCES

1. C. J. Cui, M. W. Mozur, U. E. Verre and F. N. Weltge, Unconventional and conventional hydrocarbon resource economics: A look at the fundamental differences and how countries can address the needs of unconventional resource exploitation, in *SPE Hydrocarbon Economics and Evaluation Symp.*, Houston, TX, USA, May 19–20, 2014 (Society of Petroleum Engineers, Richardson, TX, USA, 2014), doi:10.2118/169873-MS.
2. D. Alfarge, M. Wei and B. Bai, IOR methods in unconventional reservoirs of North America: Comprehensive review, in *SPE Western Regional Meeting*, Bakersfield, CA, USA, April 23–27, 2017 (Society of Petroleum Engineers, Richardson, TX, USA, 2017), doi:10.2118/185640-MS.
3. A. A. Osiptsov, Fluid mechanics of hydraulic fracturing: A review, *J. Petrol. Sci. Eng.* **156** (2017) 513–535.
4. Q. Li, H. Xing, J. Liu and X. Liu, A review on hydraulic fracturing of unconventional reservoir, *Petroleum* **1**(1) (2015) 8–15.
5. N. R. Morrow and G. Mason, Recovery of oil by spontaneous imbibition, *Curr. Opin. Colloid Interface Sci.* **6**(4) (2001) 321–337.
6. G. Mason and N. R. Morrow, Developments in spontaneous imbibition and possibilities for future work, *J. Petrol. Sci. Eng.* **110** (2013) 268–293.
7. Q. Meng, H. Liu and J. Wang, A critical review on fundamental mechanisms of spontaneous imbibition and the impact of boundary condition, fluid viscosity and wettability, *Adv. Geo-Energ. Res.* **1**(1) (2017) 1–17.
8. T. Babadagli, Analysis of oil recovery by spontaneous imbibition of surfactant solution, *Oil Gas Sci. Technol.* **60** (2005) 697–710.
9. B. F. Towler, H. L. Lehr, S. W. Austin, B. Bowthorpe, J. H. Feldman, S. K. Forbis, D. Germack and M. Firouzi, Spontaneous imbibition experiments of enhanced oil recovery with surfactants and complex nano-fluids, *J. Surfactants Deterg.* **20**(2) (2017) 367–377.
10. M. A. Fernø, Enhanced oil recovery in fractured reservoirs, in *Introduction to Enhanced Oil Recovery (EOR) Processes and Bioremediation of Oil-contaminated Sites*, ed. L. Romero-Zerón (InTech, London, UK, 2012), pp. 89–110.
11. A. Javaheri, H. Dehghanpour and J. Wood, Imbibition oil recovery from tight rocks with dual-wettability pore-network: A Montney case study, in *SPE Unconventional Resources Conf.*, Calgary, Alberta, Canada, February 15–16, 2017 (Society of Petroleum Engineers, Richardson, TX, USA, 2017), doi:10.2118/185076-MS.
12. H. Dehghanpour, Q. Lan, Y. Saeed, H. Fei and Z. Qi, Spontaneous imbibition of brine and oil in gas shales: Effect of water adsorption and resulting microfractures, *Energy Fuels* **27**(6) (2013) 3039–3049.
13. M. K. Schwiebert and W. H. Leong, Underfill flow as viscous flow between parallel plates driven by capillary action, *IEEE Trans. Compon. Packag. Technol. C* **19**(2) (1996) 133–137.
14. Y. Xiao, F. Yang and R. Pitchumani, A generalized analysis of capillary flows in channels, *J. Colloid Interface Sci.* **298**(2) (2006) 880–888.
15. J. Wang, H. Liu, J. Xia, Y. Liu, C. Hong, Q. Meng and Y. Gao, Mechanism simulation of oil displacement by imbibition in fractured reservoirs, *Petrol. Explor. Dev.* **44**(5) (2017) 805–814.
16. B. B. Mandelbrot, *The Fractal Geometry of Nature* (W. H. Freeman and Company, New York, 1982).
17. J. Cai, B.-M. Yu, M.-F. Mei and L. Luo, Capillary rise in a single tortuous capillary, *Chin. Phys. Lett.* **27**(5) (2010) 054701.
18. W. L. Power and T. E. Tullis, Euclidean and fractal models for the description of rock surface roughness, *J. Geophys. Res.* **96**(B1) (1991) 415–424.
19. J. M. Boffa, C. Allain and J. P. Hulin, Experimental analysis of fracture rugosity in granular and compact

- rocks, *Eur. Phys. J. Appl. Phys.* **2**(3) (1998) 281–289.
20. K. Develi and T. Babadagli, Quantification of natural fracture surfaces using fractal geometry, *Math. Geol.* **30**(8) (1998) 971–998.
  21. T. Babadagli and K. Develi, Fractal characteristics of rocks fractured under tension, *Theor. Appl. Fract. Mech.* **39**(1) (2003) 73–88.
  22. R. N. Wenzel, Resistance of solid surfaces to wetting by water, *Ind. Eng. Chem.* **28**(8) (1936) 988–994.
  23. J. C. Russ, *Fractal Surfaces* (Plenum Press, New York, 1994).
  24. D. L. Turcotte, *Fractals and Chaos in Geology and Geophysics*, 2nd edn. (Cambridge University Press, New York, 1997).
  25. R. D. Hazlett, Fractal applications: Wettability and contact angle, *J. Colloid Interface Sci.* **137**(2) (1990) 527–533.
  26. S. R. Brown, Fluid flow through rock joints: The effect of surface roughness, *J. Geophys. Res.* **92**(B2) (1987) 1337–1347.
  27. M. Wang, Y.-F. Chen, G.-W. Ma, J.-Q. Zhou and C.-B. Zhou, Influence of surface roughness on nonlinear flow behaviors in 3D self-affine rough fractures: Lattice Boltzmann simulations, *Adv. Water Resour.* **96** (2016) 373–388.
  28. C.-L. Cheng, E. Perfect, B. Donnelly, H. Z. Bilheux, A. S. Tremsin, L. D. McKay, V. H. DiStefano, J.-C. Cai and L. J. Santodonato, Rapid imbibition of water in fractures within unsaturated sedimentary rock, *Adv. Water Resour.* **77** (2015) 82–89.
  29. H. R. Wanless, *Pennsylvanian Geology of a Part of the Southern Appalachian Coal Field* (Geological Society of America Memoir, Boulder, CO, 1946).
  30. S. Gehne and P. M. Benson, Permeability and permeability anisotropy in Crab Orchard sandstone: Experimental insights into spatio-temporal effects, *Tectonophysics* **712/713** (2017) 589–599.
  31. B. Donnelly, E. Perfect, L. D. McKay, P. J. Lemiszki, V. H. DiStefano, L. M. Anovitz, J. McFarlane, R. E. Hale and C.-L. Cheng, Capillary pressure — saturation relationships for gas shales measured using a water activity meter, *J. Nat. Gas Sci.* **33** (2016) 1342–1352.
  32. J. D. McLennan, J. C. Roegiers and W. P. Marx, The Mancos formation: An evaluation of the interaction of geological conditions, treatment characteristics and production, in *SPE/DOE Low Permeability Gas Reservoirs Symp.*, Denver, CO, USA, March 14–16, 1983 (Society of Petroleum Engineers, Richardson, TX, USA, 1983), doi:10.2118/11606-M.
  33. U. S. Energy Information Administration, *Review of Emerging Resources: U. S. Shale Gas and Shale Oil Plays* (United States Department of Energy, Washington, DC, 2011).
  34. M. Mokhtari and A. N. Tutuncu, Characterization of anisotropy in the permeability of organic-rich shales, *J. Petrol. Sci. Eng.* **133** (2015) 496–506.
  35. D. Y. Li and L. N. Y. Wong, The Brazilian disc test for rock mechanics applications: Review and new insights, *Rock Mech. Rock Eng.* **46**(2) (2013) 269–287.
  36. C. A. Schneider, W. S. Rasband and K. W. Eliceiri, NIH Image to ImageJ: 25 years of image analysis, *Nat. Methods* **9** (2012) 671–675.
  37. A. Keller, High resolution, non-destructive measurement and characterization of fracture apertures, *Int. J. Rock Mech. Min. Sci.* **35**(8) (1998) 1037–1050.
  38. J. S. Konzuk and B. H. Kueper, Evaluation of cubic law-based models describing single-phase flow through a rough-walled fracture, *Water Resour. Res.* **40** (2004) W02402, doi:10.1029/2003WR002356.
  39. E. Perfect, C.-L. Cheng, M. Kang, H. Z. Bilheux, J. M. Lamanna, M. J. Gragg and D. M. Wright, Neutron imaging of hydrogen-rich fluids in geomaterials and engineered porous media: A review, *Earth Sci. Rev.* **129** (2014) 120–135.
  40. L. Santodonato, H. Bilheux, B. Bailey, J. Bilheux, P. Nguyen, A. Tremsin, D. Selby and L. Walker, The CG-1D neutron imaging beamline at the Oak Ridge National Laboratory High Flux Isotope Reactor, *Phys. Procedia* **69** (2015) 104–108.
  41. I. A. Eckley, P. Fearnhead and R. Killick, Analysis of changepoint models, in *Bayesian Time Series Models*, eds. D. Barber, A. T. Cemgil and S. Chiappa (Cambridge University Press, Cambridge, 2011), pp. 205–224.
  42. J. Reeves, J. Chen, X. L. Wang, R. Lund and L. Qi, A review and comparison of changepoint detection techniques for climate data, *J. Appl. Meteorol. Climatol.* **6** (2007) 900–915.
  43. C. Erdman and J. W. Emerson, A fast bayesian change point analysis for the segmentation of microarray data, *Bioinformatics* **24**(19) (2008) 2143–2148.
  44. A. Zeileis, A. Shah and I. Patnaik, Testing, monitoring, and dating structural changes in exchange rate regimes, *Comput. Stat. Data Anal.* **54**(6) (2010) 1696–1706.
  45. C. Beaulieu, J. Chen and J. L. Sarmiento, Changepoint analysis as a tool to detect abrupt climate variations, *Philos. Trans. R. Soc. A* **370** (2012) 1228–1249.
  46. D. Marquardt, An algorithm for least-squares estimation of nonlinear parameters, *J. Soc. Ind. Appl. Math.* **11**(2) (1963) 431–441.

47. W. H. Kruskal and W. A. Wallis, Use of ranks in one-criterion variance analysis, *J. Am. Stat. Assoc.* **47**(260) (1952) 583–621.
48. R Core Team, *R: A Language and Environment for Statistical Computing* (R Foundation for Statistical Computing, Vienna, Austria, 2016), <https://www.R-project.org/>.
49. T. A. Ghezzehei, Constraints for flow regimes on smooth fracture surfaces, *Water Resour. Res.* **40** (2004) W11503, doi:10.1029/2004WR003164.
50. B. N. J. Persson, On the fractal dimension of rough surfaces, *Tribol. Lett.* **54**(1) (2014) 99–106.